Front. Earth Sci. 2025, 19(4): 596–611
https://doi.org/10.1007/s11707-025-1190-x

RESEARCH ARTICLE

Enhanced storm surge simulations in Hong Kong coastal waters an atmosphere-wave-circulation coupled model under the earth system modeling framework

Jiayi PAN (✉)[1,2], Wenfeng LAI[3], Xianqiang XIA[1], Xiaoling XU[1]

1 School of Geography and Environment, Jiangxi Normal University, Nanchang 330022, China
2 Institute of Space and Earth Information Science, The Chinese University of Hong Kong, Hong Kong 999077, China
3 Department of Ocean Science, Hong Kong University of Science and Technology, Hong Kong 999077, China

Abstract Storm surges pose serious threats to densely populated coastlines and demand accurate forecasting. This study develops a fully coupled wind–wave–circulation forecasting system for Hong Kong coastal waters within the Earth System Modeling Framework (ESMF). The system integrates the Weather Research and Forecasting (WRF) model for atmospheric forcing, the Simulating Waves Nearshore (SWAN) model for wave dynamics, and the Finite-Volume Community Ocean Model (FVCOM) for ocean circulation. Validation against tide-gauge records for five typhoons, Hato (2017), Mangkhut (2018), Higos (2020), Kompasu (2021), and Saola (2023), shows that the coupled system consistently outperforms both an uncoupled ocean model and a wave–current coupled model. It achieves domain-averaged root-mean-square errors (RMSEs) of about 0.10 m, reduces errors by 31%–61% across events, and maintains high correlation coefficients (CCs). Peak surge timing generally follows north-westward storm tracks but displays irregular inter-station lags, reflecting complex local hydrodynamics. The largest improvements occur in semi-enclosed bays such as Tolo Harbour, where RMSE reductions of 0.10–0.16 m underscore the importance of wave setup, sea-state-dependent wind stress, and current–wave feedbacks. Overall, the findings confirm that full coupling is essential for reliable surge prediction in complex coastal environments, and the achieved accuracy supports near-term operational application. Remaining challenges include sensitivity to atmospheric forcing and computational demands, though advances in high-performance computing and hybrid physics–AI approaches offer promising solutions.

Received September 7, 2025; accepted October 9, 2025

E-mail: panj@cuhk.edu.hk

Keywords storm surge, water level, WRF-SWAN-FVCOM coupled model, ESMF, Hong Kong coastal waters

1 Introduction

Storm surges, defined as abnormal rises in sea level caused by atmospheric disturbances, pose serious threats to coastal communities worldwide. They are primarily driven by strong winds and low atmospheric pressure associated with tropical cyclones, including hurricanes and typhoons. The impacts are particularly severe in densely populated coastal regions, where flooding can lead to extensive economic damage, ecological degradation, and loss of life (McIvor et al., 2012; Muis et al., 2016). Accurate prediction of surge water levels is therefore essential for disaster risk reduction.

Over the past decades, a range of operational numerical models has been developed for storm surge forecasting. Among the earliest is the Sea, Lake, and Overland Surges from Hurricanes (SLOSH) model (Jelesnianski et al., 1992; Glahn et al., 2009), which solves the shallow-water equations with wind and pressure forcing to estimate coastal water-level responses. The Advanced CIRCulation (ADCIRC) model (Luettich et al., 1992) was designed to conserve mass and momentum under incompressibility, Boussinesq, and hydrostatic assumptions, enabling high-resolution coastal simulations. Other widely used systems include: the UK storm surge model (Flowerdew et al., 2013), which applies 2D shallow-water equations calibrated against tide gauges; the MIKE 21-based model (Petersen et al., 2005; Kliem et al., 2006), which employs nonlinear shallow-water dynamics with tidal, wind, and pressure forcing; the Dutch Continental Shelf Model (DCSM98)

(Gerritsen et al., 1995; Verlaan et al., 2005), which assimilates tide-gauge data via a Kalman filter and provides probabilistic forecasts with European Centre for Medium-Range Weather Forecasts (ECMWF) ensembles; and the Japan Meteorological Agency (JMA) model (Higaki et al., 2009), which produces high-resolution 33-h forecasts at nearly 300 coastal sites, updated eight times daily using mesoscale atmospheric forcing.

The performance of these systems has been verified in numerous case studies. SLOSH was validated against major historical storms, including Carla (1961), Betsy (1965), Camille (1969), and Hugo (1989), with results showing water-level predictions accurate to within ±20% (approximately 0.30 m) (Jelesnianski et al., 1992). More recently, validation against Hurricane Sandy (2012) demonstrated an overall root-mean-square error (RMSE) of about 0.47 m (Forbes et al., 2014). Hindcasts of Typhoon Saola (2023) with SLOSH in Hong Kong, China also showed average errors of 0.2–0.3 m on the day before and after Saola's closest approach (Lau et al., 2024). The ADCIRC model has been widely applied, with errors of ~0.5 m during Hurricane Katrina (Bunya et al., 2010), relative errors of 12%–14% in the South China Sea (Han et al., 2019), and 25.6 cm (14%) in China's coastal waters under accurate typhoon tracks (Liu et al., 2014). The JMA system typically maintains forecast errors within ±100 cm for lead times up to 72 h (Hasegawa et al., 2012), while DCSM98 and MIKE 21 achieve RMSEs of 15–25 cm and 10–30 cm, respectively (Cañizares et al., 2001; Verlaan et al., 2005).

Although these 2D models are efficient for operational use, their simplified formulations omit key processes involving wind, waves, and circulation interactions, which limits their accuracy, especially during surge peaks and in areas with complex coastal morphology. Achieving higher accuracy is generally challenging under such simplifications, and uncertainties in wind forcing further constrain forecasts. Recent advances underscore the advantages of fully coupled models that integrate atmospheric, hydrodynamic, and wave dynamics, providing a more complete representation of extreme-event processes (Qi et al., 2009; Tasnim et al., 2014; Luo et al., 2021; Li and Chen, 2022; Leung et al., 2024; Li et al., 2024; Zhang et al., 2025).

In this study, we develop a fully coupled wind–wave–circulation storm surge model within the Earth System Modeling Framework (ESMF) and apply it to Hong Kong coastal waters, which are highly affected by tropical cyclones and storm surges, particularly in summer and autumn. Between 1954 and 2022, more than 370 storm surge events were recorded in the region, nearly 25% of which produced water-level rises exceeding 1.0 m (Sun and Pan, 2023). Using available storm surge observations for validation, we also configure and compare a direct wind-driven circulation model and a two-way wave–circulation coupled model. The results demonstrate that the fully coupled wind–wave–circulation system yields superior accuracy and represents a feasible framework for operational forecasting in complex coastal environments.

2 Methodology

In this study, a fully coupled wind-wave-circulation modeling framework is developed, which integrates the Weather Research and Forecasting (WRF) model for atmospheric forcing, the Simulating Waves Nearshore (SWAN) model for wave dynamics, and the Finite-Volume Community Ocean Model (FVCOM) for ocean circulations.

2.1 Atmospheric model

The Weather Research and Forecasting (WRF) model is employed to simulate winds and generate atmospheric forcing for the FVCOM simulations, providing high spatial and temporal resolution meteorological inputs (Michalakes et al., 1998). As a next-generation mesoscale numerical weather prediction system, WRF is designed to meet both operational forecasting and atmospheric research needs. It uses a fully compressible, non-hydrostatic dynamical core, with an Arakawa C-grid in the horizontal direction and terrain-following vertical coordinates, making it well suited for resolving fine-scale atmospheric processes over complex terrain and coastal environments.

To enhance spatial detail, a dynamical downscaling approach is applied, allowing the model to capture the effects of complex topography and land-sea-air interactions. A three-domain nested configuration is adopted (Fig. 1(a)). The outer domain (D01) encompasses the western Pacific Ocean, the entire China Sea, and the Sea of Japan, with a horizontal resolution of 9 km. The second domain (D02) focuses on the northern South China Sea (NSCS) with a 3 km resolution, while the innermost domain (D03) covers the Guangdong-Hong Kong-Macao Greater Bay Area and the Pearl River Estuary (PRE) at a 1 km resolution, fully encompassing the FVCOM model domain.

All three domains contain 33 vertical layers, extending to a model top pressure of 50 hPa. Initial and lateral boundary conditions for the outer domain are derived from the fifth-generation atmospheric (ERA5) reanalysis data provided by the European Centre for Medium-Range Weather Forecasts (ECMWF). The model physics suite includes the WSM6 microphysics scheme, the Rapid Radiative Transfer Model (RRTM), the Dudhia shortwave radiation scheme, the Yonsei University (YSU) planetary boundary layer scheme, and the Kain-Fritsch cumulus parameterization (Skamarock et al., 2019).

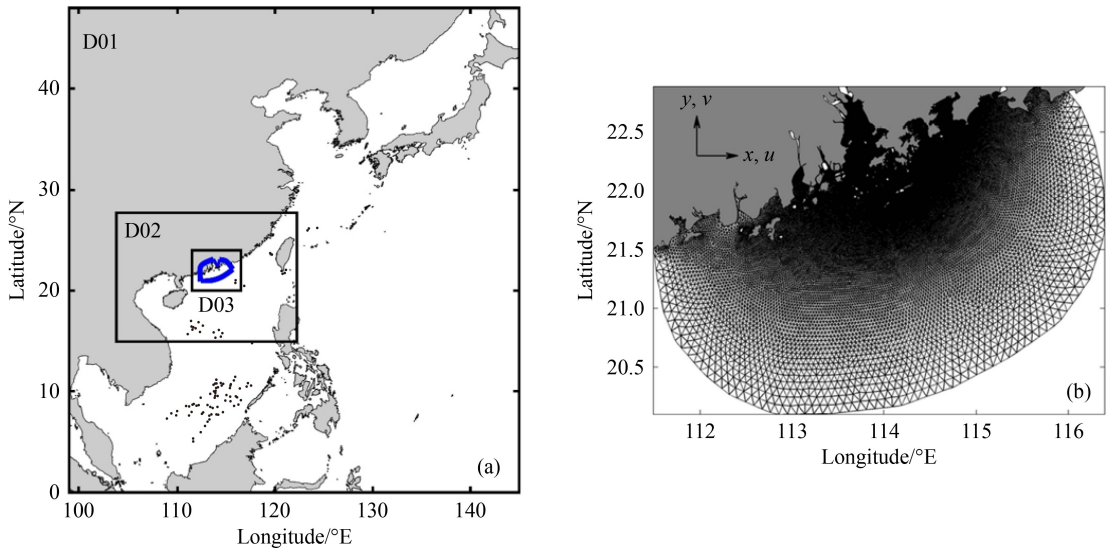

Fig. 1 The model domains of the (a) WRF, (b) FVCOM, and (c) SWAN models.

2.2 Wave model

For wave simulations, we employ the Simulating Waves Nearshore (SWAN) model, a third-generation numerical wave model designed to compute random, short-crested, wind-generated waves in coastal regions and inland waters. SWAN is one of the most widely used surface wave models, with extensive applications in coastal ocean wave forecasting, engineering design, and research (Booij et al., 1999).

The model can simulate a comprehensive range of wave processes, including wave propagation in time and space, shoaling, and refraction caused by both bathymetry and mean currents. It also accounts for frequency shifting due to currents and changes in water depth, wave generation by wind, bottom friction, depth-induced breaking, and wave transmission through or reflection from obstacles. The primary inputs to SWAN include a bathymetric grid, incident wave spectra at the model boundaries, wind fields for wind-wave generation, and mean current velocities for current-induced refraction.

In this study, SWAN and FVCOM are coupled on the same computational grid to ensure consistency in spatial representation (Fig. 1(b)). Wave conditions at the open boundary are obtained from the NOAA WAVEWATCH III global model, which provides outputs at a spatial resolution of 0.5° and a temporal resolution of three hours. This coupling allowed the simulations to capture both large-scale wave conditions and fine-scale coastal wave transformations within the study domain.

2.3 Ocean circulation model

FVCOM is a prognostic, three-dimensional (3D), free-surface, primitive equation ocean model, in which, the horizontal grid is composed of unstructured triangular cells, while the vertical structure is represented using terrain-following coordinates to capture realistic topography (Chen et al., 2003, 2006). One of the model's greatest strengths lies in its geometric flexibility: the unstructured triangular mesh allows it to accurately conform to complex and irregular coastal boundaries. Figure 1(b) illustrates the unstructured triangular grids of FVCOM and the wave models for the Pearl River Estuary (PRE) and surrounding coastal waters. The model domain, spanning 111.5°E −116.5°E and 20°N −23°N, encompasses the entire PRE with an open boundary in the northern South China Sea. The grid contains 41,027 nodes and 78,539 cells, with horizontal resolutions ranging from 0.1 to 10 km: 0.1 to 0.3 km within the estuary, 0.3 to 0.5 km at the estuary mouth, 1.0 to 2.0 km in Guangdong coastal waters, and 10 km near the open boundary. In Hong Kong coastal waters, the spatial resolution is around 0.1 km. Vertically, the model employs 20 uniform hybrid terrain-following layers.

Tidal forcing is applied at the open boundary using eight primary tidal constituents (M2, N2, S2, K2, K1, O1, P1, and Q1), derived from the (1/6)° inverse tidal model results of Egbert and Erofeeva (2002). In addition, salinity, temperature, and velocity conditions at the open boundary are taken from the Hybrid Coordinate Ocean Model (HYCOM). On the landward side, monthly mean freshwater discharges from eight river inlets provide lateral boundary conditions. The model uses a split-mode time-stepping scheme, with a 1-s external time step and a split factor of 5, to integrate the equations. Wet/dry treatment is included to account for tidal inundation in upstream coastal areas. Vertical mixing is parameterized with the Mellor-Yamada level 2.5 (MY-2.5) scheme, while horizontal mixing uses the Smagorinsky formulation (Mellor and Yamada, 1982).

2.4 Model coupling strategies and mechanisms

2.4.1 Uncoupled model

In this study, three different strategies are used to examine wind-wave-circulation interactions. The first approach is the uncoupled system (FVCOM and SWAN) with one-way WRF forcing. In this configuration, FVCOM and SWAN operate as a standalone models driven solely by atmospheric fields from WRF, without coupling between and circulation and wave models. This serves as a baseline case for evaluating the added value of including wave coupling and fully integrated system coupling in storm surge predictions (Fig. 2(a)). In this setup, the WRF model generates wind and atmospheric pressure fields, which are directly applied as forcing to FVCOM and SWAN. However, there is no feedback between the models-FVCOM and SWAN receive the atmospheric forcing independently, and the ocean model does not influence the atmospheric simulation.

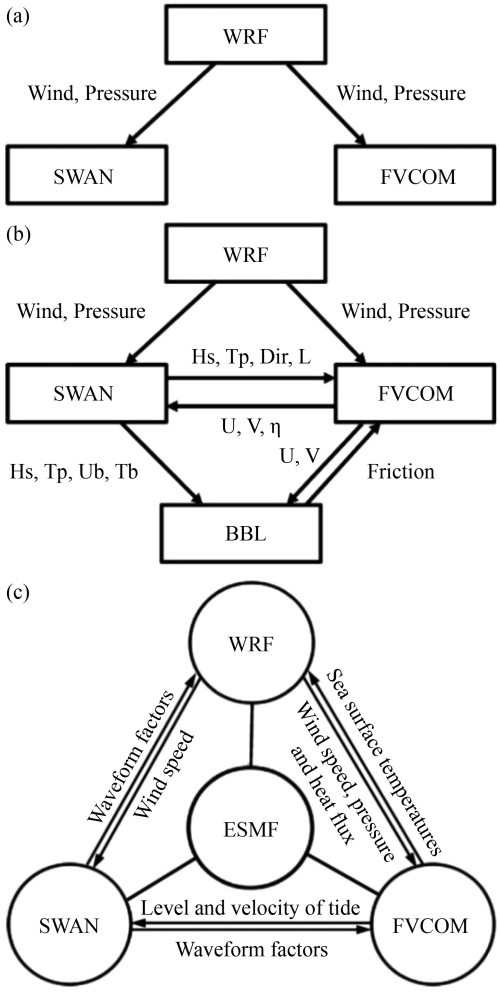

Fig. 2 Three strategies of the (a) wind-wave-circulation coupling: uncoupled model, (b) wave-circulation coupled model, and (c) wind-wave-circulation fully coupled model.

2.4.2 Wave-circulation coupled model

The second approach is a partially coupled system (FVCOM + SWAN) with WRF forcing (Fig. 2(b)). In this configuration, FVCOM and SWAN are fully two-way coupled to capture wind-circulation interactions, while WRF still operates independently, providing atmospheric forcing without receiving feedback from the ocean or wave models. This design allows us to assess the importance of coupled wave-circulation dynamics.

In this setup, FVCOM and SWAN share the same unstructured triangular grid (Fig. 1(b)), minimizing interpolation errors and improving computational efficiency. The two-way coupling allows vertically sheared currents from FVCOM to influence the wave field in SWAN. Figure 2(b) illustrates the schematic of the fully current-wave-bottom boundary layer (BBL) coupling system. After initialization, SWAN computes wave parameters including significant wave height (Hs), mean direction (Dir), mean wavelength (L), relative peak period (Tp), bottom orbital velocity (Ub), and bottom wave period (Tb). These wave characteristics are then used to calculate radiation or surface stress, which is passed to the circulation model. Once both models complete their respective calculations, the wave parameters, current fields, and bed parameters are provided to the BBL module. This module estimates bottom stresses under the combined influence of waves and currents, which are then applied in the ocean model's momentum equations. The circulation model outputs, current velocities and surface elevations, are subsequently fed back into the wave model, allowing SWAN to update wave fields for the next time step (Qi et al., 2009).

2.4.3 Wind-wave-circulation fully coupled model

The third and most comprehensive strategy is the fully coupled system (FVCOM + SWAN + WRF) (Fig. 2(c)). In this configuration, all three models interact dynamically, enabling complete feedback among atmospheric, oceanic, and wave processes. The Weather Research and Forecasting (WRF) model exchanges data bidirectionally with both the FVCOM ocean model and the SWAN wave model, allowing for a more realistic representation of air-sea interactions during events such as typhoons (Qi et al., 2009; Li and Chen, 2022).

The WRF-SWAN-FVCOM system incorporates multiple physical processes to capture the complexities at the air-sea interface. From the atmosphere to the ocean, the coupling transfers wind stress, heat flux, precipitation minus evaporation, and sea level pressure. In return, the ocean provides sea surface temperature (SST) to the atmospheric model as a lower boundary condition. When surface waves are included, wave parameters directly affect the calculation of wind stress, while wave-induced surface roughness, derived from significant wave height,

wavelength, and wave period, modifies the marine boundary layer parameterization in WRF. The coupling mechanism between FVCOM and SWAN is the same as described in the previous section.

Unlike the wave-circulation coupled model, the fully coupled atmosphere-wave-circulation system integrates WRF, FVCOM, and SWAN using the Earth System Modeling Framework (ESMF). ESMF not only facilitates data exchange between components but also orchestrates their execution, allowing WRF and SWAN-FVCOM to run as coordinated subroutines within a unified system. This framework provides a modular architecture for building complex modeling systems, offering standardized interfaces, regridding tools, time management utilities, logging, error handling, and parallel communication capabilities (Hill et al., 2004). Its design principle is to decompose large applications into interchangeable software components, representing physical domains, couplers, or I/O systems, which can be flexibly combined into different applications. ESMF supports both one-way and two-way coupling across models, regardless of grid type, enabling robust and scalable coupled simulations.

2.5 ESMF coupling for WRF, SWAN, and FVCOM

To enable communication between WRF and FVCOM through the Earth System Modeling Framework (ESMF), both models require targeted modifications to their coupling interfaces. These adjustments ensure that the necessary variables can be exchanged seamlessly and that data transfer between the models is fully compatible with ESMF standards (Masson et al., 2025).

For WRF, the process begins with compiling the model with ESMF support, achieved either by adding the appropriate ESMF flags to the build configuration or by using a WRF version that already supports ESMF integration. The model must be run in ESMF driver mode so that it can operate as a component within the coupled framework. In this setup, key coupling variables, such as wind, atmospheric pressure, heat flux, and sea surface temperature (SST), are explicitly defined for data exchange.

Similarly, FVCOM must be configured as an ESMF component. This involves implementing initialization and finalization routines consistent with ESMF requirements and defining the fields to be exchanged with WRF, including ocean currents, SST, and, when applicable, wave parameters from SWAN. FVCOM must also be capable of reading and writing data in ESMF-compatible formats.

Once model compatibility is established, the coupling fields exchanged between WRF and FVCOM are clearly specified. Typically, WRF provides FVCOM with atmospheric inputs such as wind stress, heat flux, and sea level pressure, while FVCOM returns oceanic variables, including SST and surface currents, to WRF. When the two models use different grids, ESMF's regridding and interpolation capabilities, such as bilinear or nearest-neighbor mapping, are applied to ensure accurate spatial alignment of data.

An ESMF coupler component is then developed to manage data flow, synchronization, and field mapping between the models. This coupler defines the exchange intervals according to the temporal and spatial scales of the application and, if necessary, generates an exchange grid to reconcile differences in model resolution.

The ESMF driver script orchestrates the coupling process. It initializes WRF and FVCOM within the ESMF framework, controls their execution sequence, handles time-stepping and data exchanges, and ensures that both models remain synchronized throughout the simulation. Typically, ESMF manages model timing and progression automatically.

Following configuration, both WRF and FVCOM are compiled with ESMF integration, and a run script is created to launch the ESMF driver alongside the coupled models. Once the system executes successfully, validation is carried out by comparing simulation outputs with observational data. If needed, coupling variables, exchange intervals, or interpolation methods are adjusted to enhance performance and accuracy.

3 Storm surge cases and tidal gauge stations

3.1 Typhoon cases

The test sites for evaluating the coupled storm surge model are located in Hong Kong coastal waters, an area frequently affected by tropical cyclones during the summer season. In this study, we selected several high-impact typhoon and super typhoon events that significantly influenced these waters: Typhoon Hato (2017), Super Typhoon Mangkhut (2018), Typhoon Higos (2020), Typhoon Kompasu (2021), and Super Typhoon Saola (2023). The basic characteristics of these storms are summarized in Table 1.

As shown in Table 1, Typhoon Hato impacted Hong Kong, China from 20 to 24 August 2017, reaching a maximum wind speed of 185 km/h (Fig. 3(a)). Super Typhoon Mangkhut affected the region from 7 to 17 September 2018 (Fig. 3(b)), while Typhoon Higos struck from 17 to 19 August 2020 (Fig. 3(c)). Typhoon Kompasu occurred between 8 and 14 October 2021 (Fig. 3(d)), and Super Typhoon Saola impacted the area from 23 August to 3 September 2023 (Fig. 3(e)).

Among these events, Mangkhut (2018) and Saola (2023) were classified as super typhoons, Hato (2017) was a severe typhoon, and Higos (2020) and Kompasu (2021) were categorized as typhoons. These storms

Table 1 The typhoon info. of Hato (2017), Mangkhut (2018), Higos (2020), Kompasu (2021), and Saola (2023)*

Year	Name	Period of influence (Hong Kong, local time)	Closest approach (local time/ distance and direction)	Max sustained winds near center/(km•h^{-1})
2017	Hato	20−24 Aug 2017	23 Aug 10:00, ~60 km SSW of HKO	185
2018	Mangkhut	7−17 Sep 2018	16 Sep 13:00, ~100 km SSW of HKO	250
2020	Higos	17−19 Aug 2020	19 Aug 05:00, ~80 km WSW of HKO	130
2021	Kompasu	8−14 Oct 2021	13 Oct 04:00, ~360 km south of HKO	120
2023	Saola	23 Aug−3 Sep 2023	1 Sep 21:00, ~40 km SSE of HKO	230

Notes: *The table data were obtained from Hong Kong Observatory Web

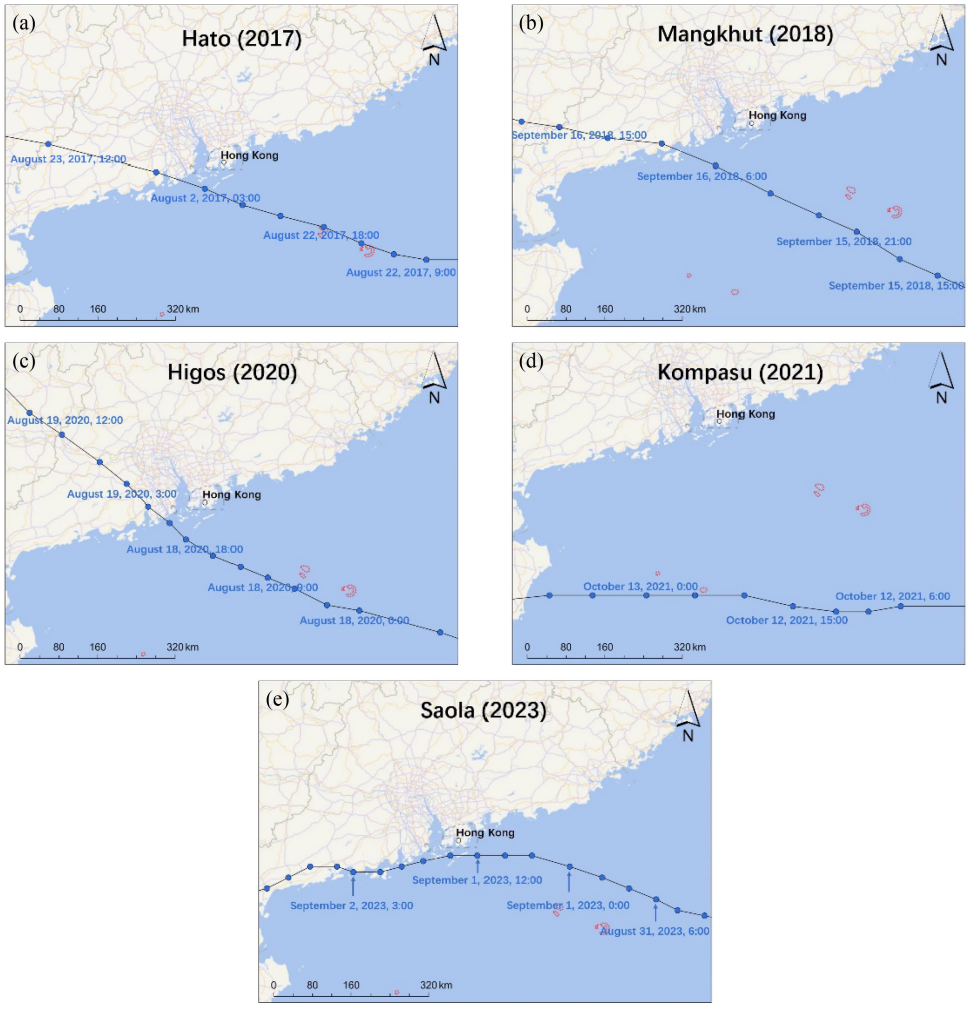

Fig. 3 Typhoon tracks for (a) Typhoon Hato (2017), (b) Super Typhoon Mangkhut (2018), (c) Typhoon Higos (2020), (d) Typhoon Kompasu (2021), and (e) Super Typhoon Saola (2023).

represent some of the most significant tropical cyclone events in recent years for Hong Kong, China, producing strong storm surge and water level responses. Their selection provides an optimal set of cases for testing and validating storm surge model performance in the region.

3.2 Surged water levels

The water levels recorded at several Hong Kong tidal gauge stations are used to evaluate the model performance. These stations, Tsim Bei Tsui, Tai Po Kau, Quarry Bay, Tai Miu Wan, Tai O, and Shek Pik are located across the eastern, south-western, and western coastal waters surrounding Hong Kong, China (Fig. 4). The water levels are obtained from Hong Kong Observatory. Their spatial distribution provides coverage of distinct hydrodynamic environments, allowing the assessment of how water levels respond to strong typhoon winds in different parts of the region.

Because the stations occupy varied locations and

Fig. 4 Hong Kong Tidal Gauge Stations.

exposure conditions, they exhibit different magnitudes and timings of storm surge responses. To quantify these effects, the maximum water level increases, defined as the absolute storm surge height obtained by removing the astronomical tidal component from the observed total water level, were determined for each site. Table 2 lists these maximum surge values along with the corresponding dates and times of occurrence, providing a benchmark for comparison with model simulations.

During Hato (2017), the earliest maximum water level increase was recorded at 07:53 on August 23 (local time) at Tai Miu Wan Station, followed by Quarry Bay at 10:27. Tai Po Kau reached its peak at 10:58. Shek Pik experienced its maximum at 11:32, and finally Tsim Bei Tsui at 13:42, but with the highest value among all stations (2.42 m). The time intervals between stations were irregular relative to their spatial distances in the north-westward direction. From Tai Miu Wan to Quarry Bay, the lag was 1 h 34 min; from Quarry Bay to Tai Po Kau, only 31 min. The longest interval occurred between Tai Miu Wan and Quarry Bay, whereas much shorter intervals were observed between Quarry Bay and Tai Po Kau, and between Shek Pik and Tsim Bei Tsui. Similar irregularities in timing were also found in other typhoon surge cases.

In the case of Mangkhut (2018), the first maximum water level increase appeared at Tai Po Kau at 12:34 on September 16, with the highest value (3.40 m) among all stations. The subsequent peaks occurred at Tai Miu Wan (13:41), Shek Pik (14:16), Quarry Bay (14:42), and finally Tsim Bei Tsui (17:21). The lag between Tai Miu Wan and Quarry Bay was longer than that between Tai Miu Wan and Shek Pik. As in Hato, the latest arrival of the maximum water-level increase was again observed at Tsim Bei Tsui.

For Higos (2020), the sequence began at Tai Po Kau at 00:57 on August 19, followed by Quarry Bay (03:48), Tai Miu Wan (04:49), Shek Pik (05:26), and finally Tsim Bei

Table 2 Maximum water level increase at 5 tidal gauge stations for Hato (2017), Mangkhut (2018), Higos (2020), Kompasu (2021), and Saola (2023)*

Stations	Hato (2017)		Mangkhut (2018)		Higos (2020)		Kompasu (2021)		Saola (2023)	
	Max sea level increase/m	Data and Time (HKT)	Max sea level increase/m	Data and Time (HKT)	Max sea level increase/m	Data and Time (HKT)	Max sea level increase/m	Data and Time (HKT)	Max sea level increase/m	Data and Time (HKT)
Tai Miu Wan	1.05	2017-08-23 07:53	2.77	2018-09-16 13:41	0.64	2020-08-19 04:49	1.21	2021-10-13 08:42	0.91	2023-09-01 22:45
Quarry Bay	1.18	2017-08-23 10:27	2.35	2018-09-16 14:42	0.51	2020-08-19 03:48	1.13	2021-10-13 08:49	0.76	2023-09-01 23:50
Tai Po Kau	1.65	2017-08-23 10:58	3.40	2018-09-16 12:34	0.61	2020-08-19 00:54	1.16	2021-10-13 07:57	1.48	2023-09-01 21:57
Shek Pik	1.54	2017-08-23 11:32	2.34	2018-09-16 14:16	0.71	2020-08-19 05:26	1.36	2021-10-13 09:32	0.72	2023-09-02 04:40
Tsim Bei Tsui	2.42	2017-08-23 13:42	2.58	2018-09-16 17:21	1.02	2020-08-19 07:43	1.27	2021-10-13 10:59	0.73	2023-09-02 04:11

Note: *The table data were obtained from Hong Kong Observatory Web

Tsui (07:43). Unlike Hato and Mangkhut, the maximum appeared earlier at Quarry Bay than at Tai Miu Wan. Moreover, Tsim Bei Tsui recorded the highest maximum water-level increase (1.02 m) among all stations.

With Kompasu (2021), the earliest maximum was recorded at Tai Po Kau at 07:57 on October 13, followed by Tai Miu Wan (08:42), Quarry Bay (08:49), and Shek Pik (09:32). The latest maximum occurred at Tsim Bei Tsui at 10:59. The highest increase (1.36 m) was observed at Shek Pik.

Finally, during Saola (2023), Tai Po Kau experienced the earliest maximum water-level increase at 21:57 on September 1, followed by Tai Miu Wan (22:45) and Quarry Bay (23:50). On the following day, Tsim Bei Tsui and Shek Pik reached their maxima at 04:11 and 04:40, respectively. The highest water-level increase (1.48 m) was observed at Tai Po Kau.

Across all five typhoons, Tai Po Kau and Tai Miu Wan frequently exhibited the earliest arrival of maximum water-level increases, while Tsim Bei Tsui consistently recorded the latest peaks. Since all the typhoon cases moved north-westward, the maximum water levels generally appeared in an order aligned with the typhoon tracks (Fig. 4), revealing that the surged seawater was advected north-westward under the influence of these storms. The highest values varied among stations and events, with Tai Po Kau registering the largest increases during Mangkhut (3.40 m) and Saola (1.48 m), while Shek Pik recorded the highest during Kompasu (1.36 m), and Tsim Bei Tsui during Hato (2.42 m) and Higos (1.02 m). Generally, Tai Po Kau and Tsim Bei Tsui were prone to experiencing the highest water-level increases, which may be attributed to their bay morphology, where the enclosed coastal configuration enhances surge amplification. The irregular timing between adjacent stations, sometimes longer between closer sites and shorter between more distant ones, highlights the complex interplay of storm track, wind forcing, and coastal topography in shaping surge dynamics.

4 Results

In this study, we implement three wind-wave-circulation coupling strategies to compare their performance. The first is the uncoupled model, where only wind forcing is applied to the ocean circulation model (Strat. 1). The second is the wave-current coupled model, with wind forcing applied to both wave and current interactions (Strat. 2). The third is the fully coupled wind-wave-

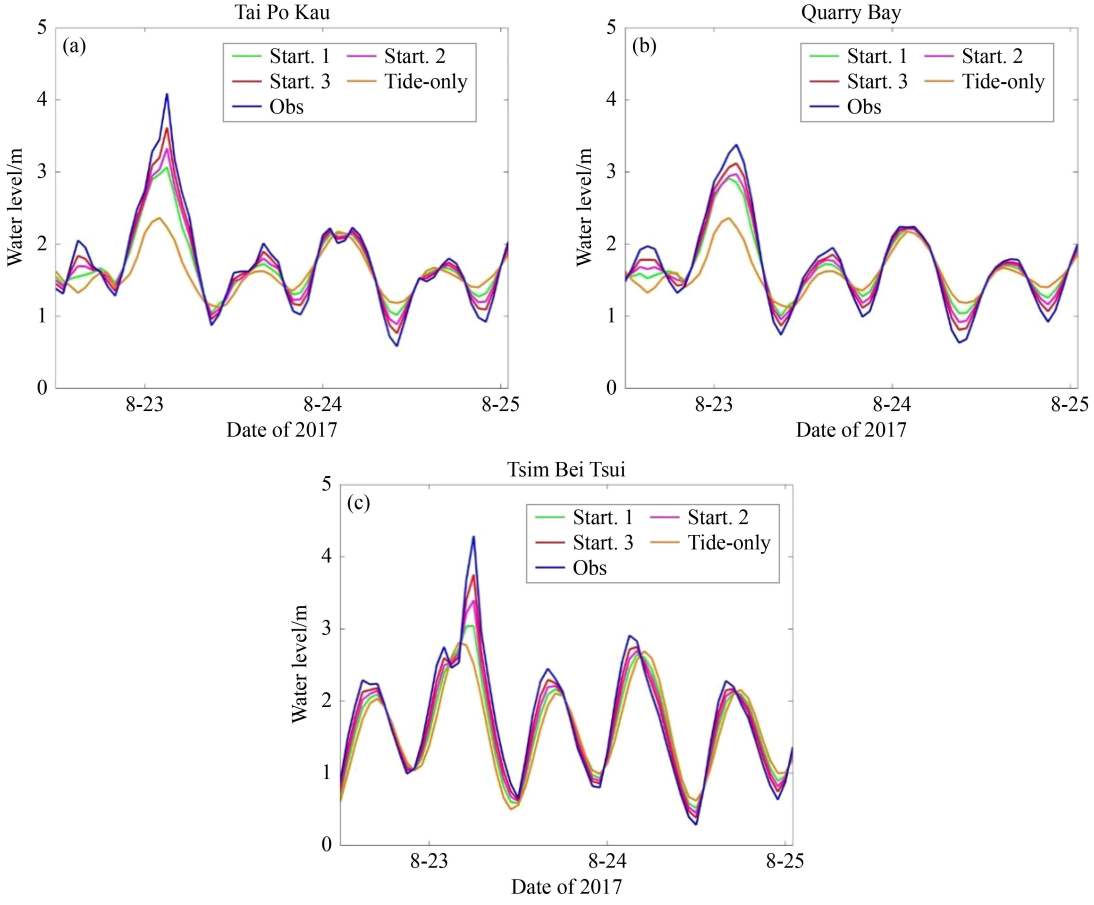

Fig. 5 Water levels during typhoon Hato (2017) at (a) Tai Po Kau, (b) Quarry Bay, and (c) Tsim Bei Tsui.

current model (Strat. 3). All three strategies were applied to the five selected typhoon cases.

To quantitatively assess model performance, simulated sea levels were compared against observational data from multiple tide gauge stations. Model validation was carried out using hourly tide gauge measurements (Figs. 5−9). Two statistical metrics were employed for evaluation.

1) Root-Mean-Squared Error (RMSE): quantifies the absolute deviation between model simulations and observations.

2) Correlation Coefficient (CC): measures the strength and consistency of the temporal relationship between simulated and observed values.

Together, these metrics provide a comprehensive assessment of predictive skill, capturing both the accuracy of the water-level magnitudes and the model's ability to reproduce temporal variations in sea-level dynamics. The simulated water levels for the five typhoon events are shown in Figs. 5−9: Hato (2017), Mangkhut (2018), Higos (2020), Kompasu (2021), and Saola (2023).

In these figures, the blue lines re present the observed water levels. Among the three strategies, Strat. 3 reproduces the observations most accurately, followed by Strat. 2, while Strat. 1 shows the largest deviations. The fully coupled model is particularly effective in capturing the peak water levels within tidal cycles. Differences among the strategies are most evident during surge peaks, whereas discrepancies at mean water levels remain relatively minor. A quantitative comparison is provided in Tables 3−7, which summarize the RMSE and CC values between simulated and observed water levels across the tide gauge stations.

Across the five typhoon cases, a clear hierarchy emerges among the three coupling strategies. The uncoupled model (Strat. 1) persistently yields the largest RMSEs, the wave-current coupled system (Strat. 2) shows moderate improvement, and the fully coupled approach (Strat. 3) consistently achieves the lowest errors. For Hato (2017) (Table 3), the RMSE decreases from 0.28 m in Strat. 1 to 0.20 m in Strat. 2, and further to 0.13 m in Strat. 3. Mangkhut (2018) follows a similar progression, with values of 0.22, 0.18, and 0.15 m (Table 4). Higos (2020) demonstrates the most pronounced improvement (Table 5), dropping from 0.15 m under Strat. 1 to 0.11 m under Strat. 2 and only 0.08 m under Strat. 3. During Kompasu (2021) (Table 6), the fully coupled setup again reduces the RMSE (0.11 m), compared with 0.19 m and 0.13 m for Strats. 1 and 2. The most striking contrast occurs in Saola (2023) (Table 7),

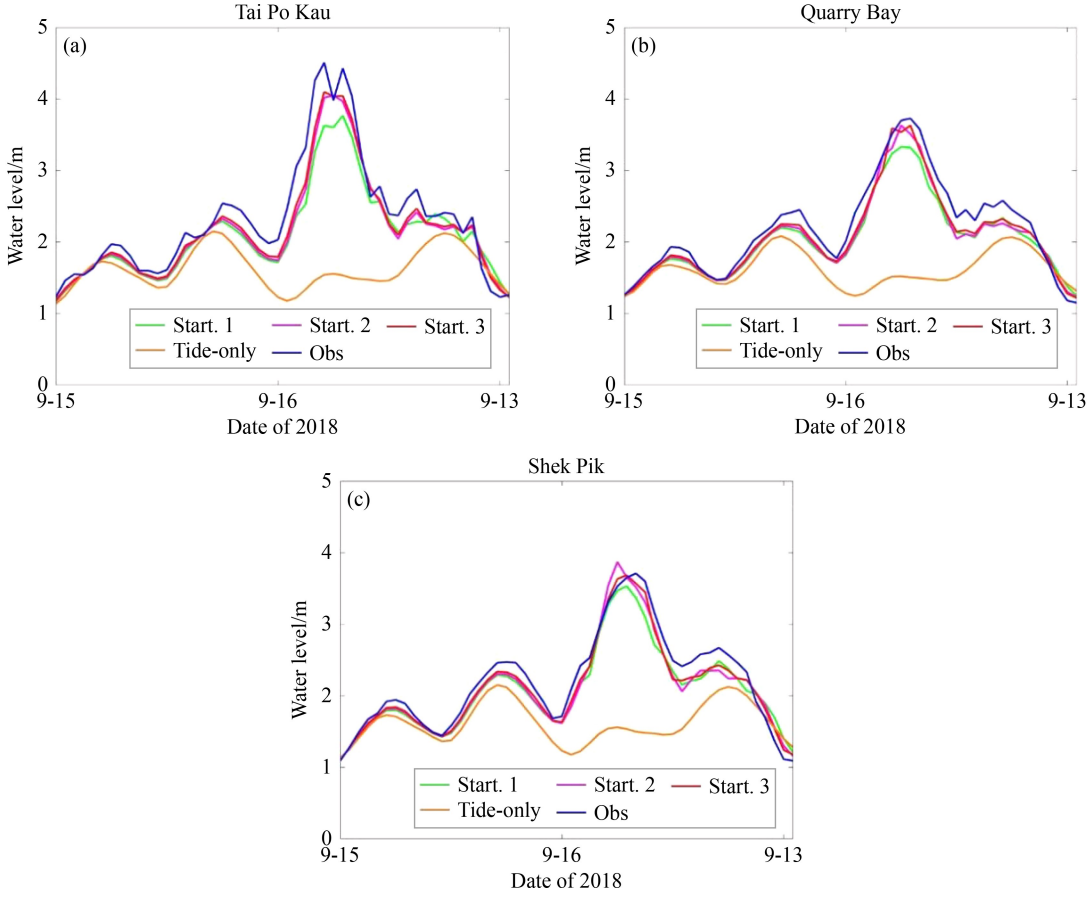

Fig. 6 Water levels during Super Typhoon Mangkhut (2018) at (a) Tai Po Kau, (b) Quarry Bay, and (c) Shek Pik.

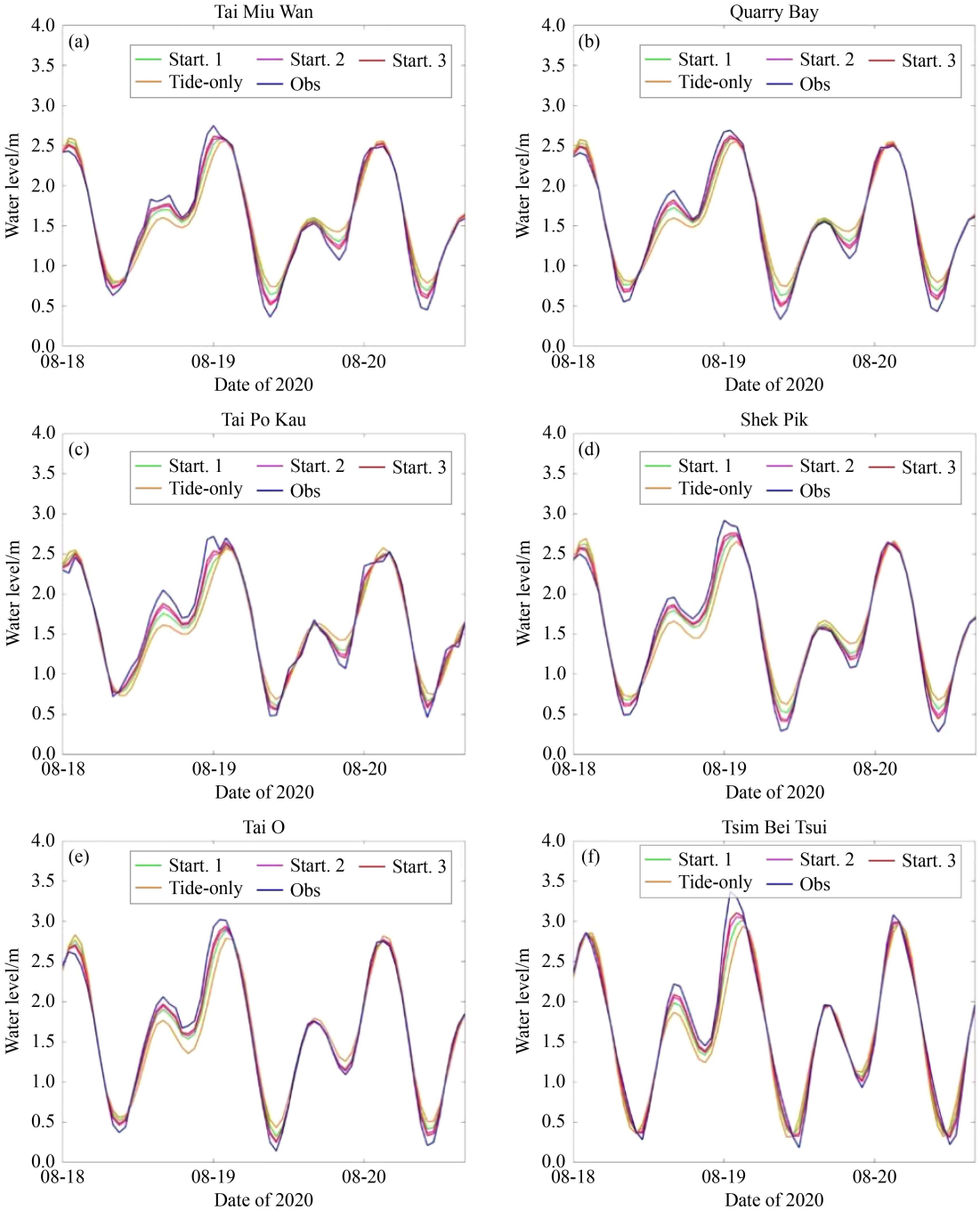

Fig. 7 Water levels during Typhoon Higos (2020) at (a) Tai Miu Wan, (b) Quarry Bay, (c) Tai Po Kau, (d) Shek Pik, (e) Tai O, and (f) Tsim Bei Tsui.

where Strat. 3 produces an RMSE of just 0.09 m, in comparison with 0.22 m and 0.15 m from the other two approaches.

The aggregated statistics in Tables 3−7 reinforce this pattern. Strat. 1, driven solely by wind forcing, cannot capture many of the hydrodynamic interactions responsible for surge amplification, particularly during peak conditions. Introducing wave-current coupling in Strat. 2 provides partial improvement, indicating that wave-induced stresses and setup are important factors. However, the superior performance of Strat. 3 demonstrates that a fully interactive wind-wave-current system is necessary to represent the complex feedback mechanisms governing storm surge. These include not only wave-induced momentum flux but also the influence of currents on wave growth and the modulation of wind stress by sea-state conditions.

The improvements are especially obvious at Tai Po Kau station, located inside Tolo Harbour on Hong Kong's east coast. This site is semi-enclosed, with narrow bathymetry

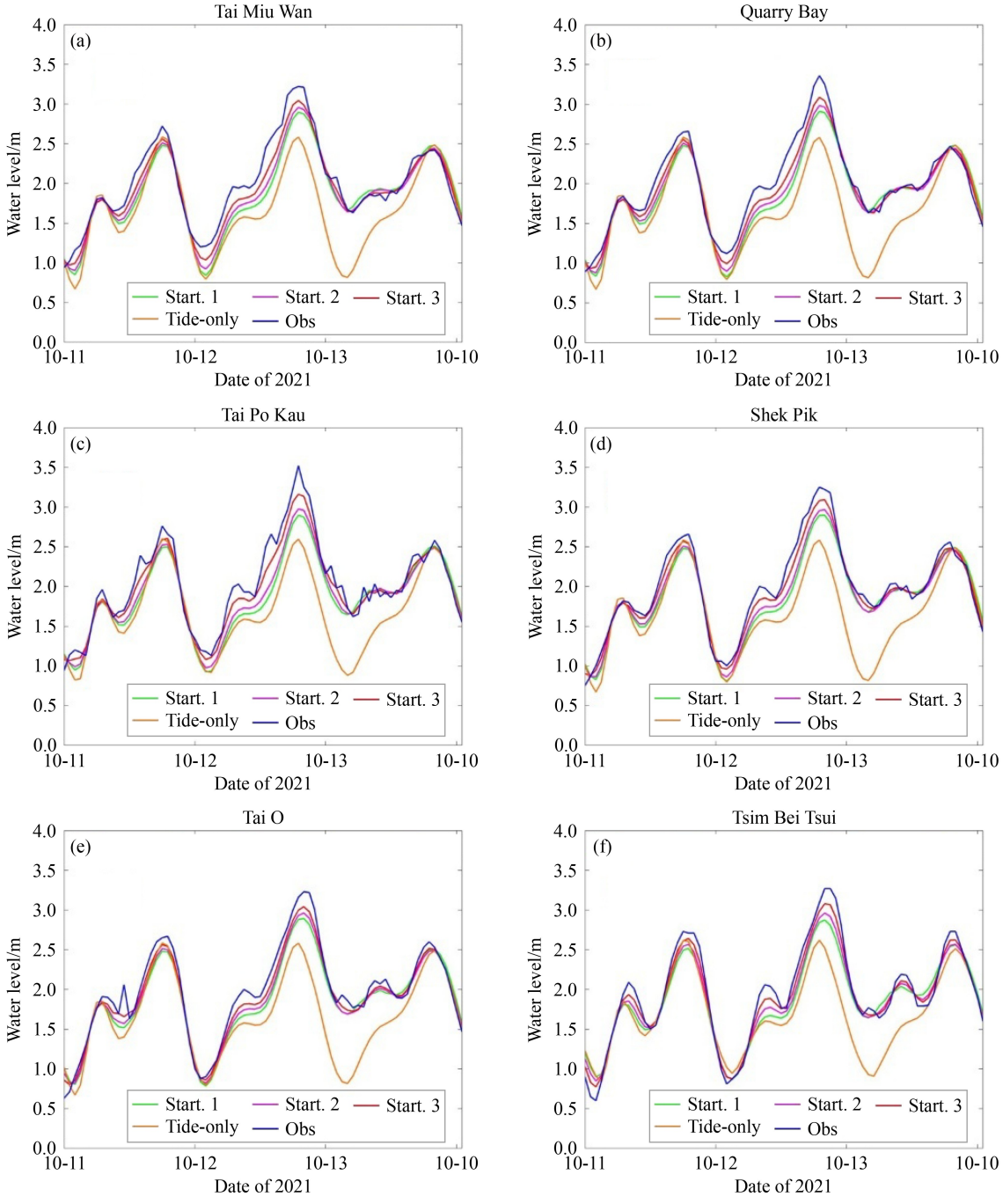

Fig. 8 Water levels during Typhoon Kompasu (2021) at (a) Tai Miu Wan, (b) Quarry Bay, (c) Tai Po Kau, (d) Shek Pik, (e) Tai O, and (f) Tsim Bei Tsui.

and restricted exchange with the open sea. Such conditions amplify the importance of coupled processes: for Mangkhut (2018), Kompasu (2021), and Saola (2023), Strat. 1 produces RMSEs of 0.27 m, 0.23 m, and 0.27 m, respectively, whereas Strat. 3 reduces them to 0.18 m, 0.13 m, and 0.11 m. The corresponding improvements, with 0.14, 0.10, and 0.16 m, are considerably larger than those at other stations. This suggests that in narrow or semi-enclosed bays, the interplay of reflected waves, confined currents, and locally enhanced wind forcing intensifies the need for a fully coupled framework.

From a broader perspective, the quantitative gains are substantial. On average across all stations, Strat. 3 reduces RMSE relative to Strat. 1 by 52.6% for Hato (2017), 31.3% for Mangkhut (2018), 43.0% for Higos (2020), 42.4% for Kompasu (2021), and 60.5% for Saola (2023). These percentages illustrate not only a consistent benefit but also case-to-case variability, implying that the extent of improvement depends on storm characteristics (e.g., track, intensity, angle of approach) and local

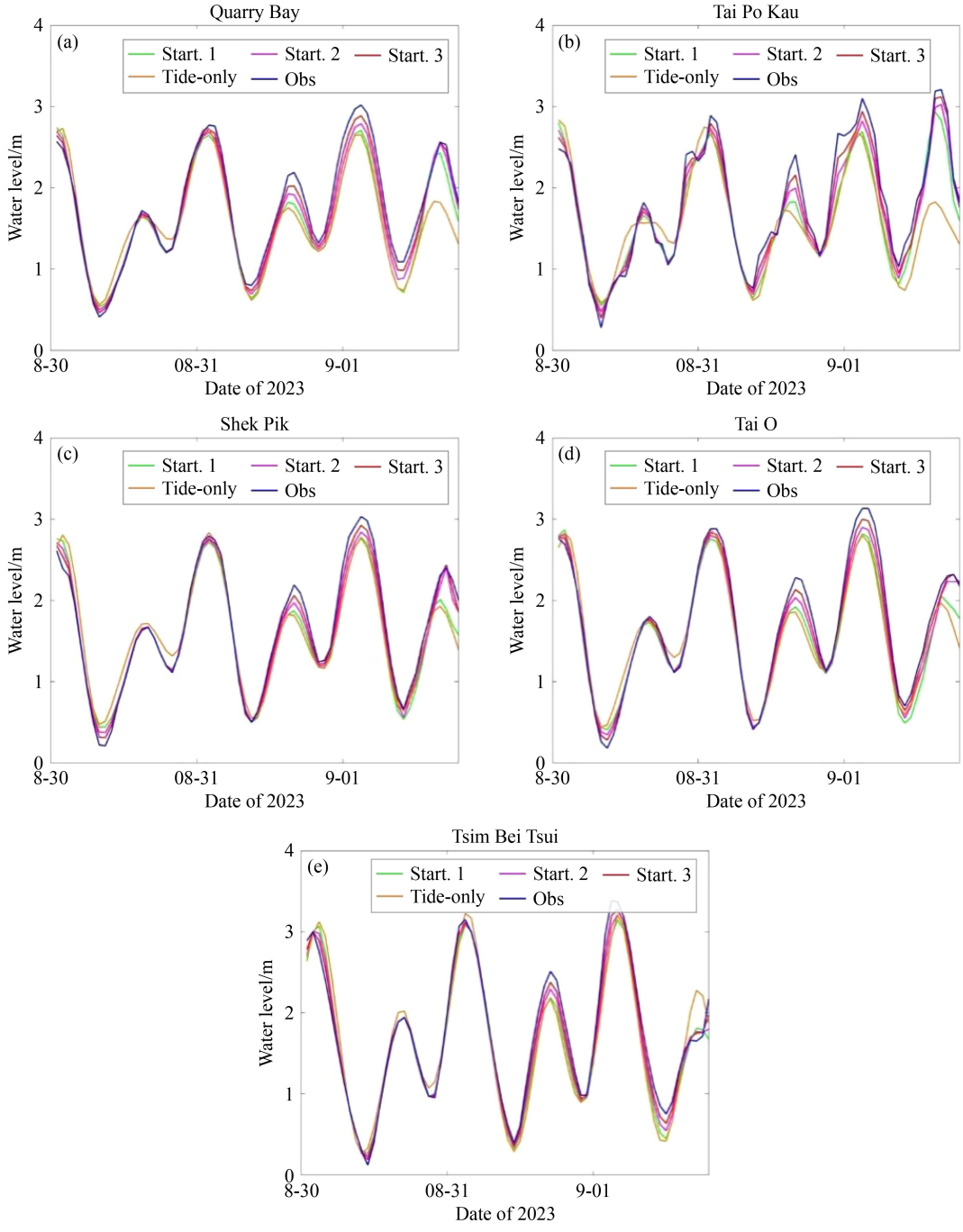

Fig. 9 Water levels during Super Typhoon Saola (2023) at (a) Quarry Bay, (b) Tai Po Kau, (c) Shek Pik, (d) Tai O, and (e) Tsim Bei Tsui.

geomorphological settings. Stronger or slower-moving typhoons may create conditions where wave-current-wind feedbacks dominate, while weaker or faster systems may be less sensitive.

Overall, the model comparison underscores that a fully coupled approach is not merely an incremental refinement, but a fundamental requirement for accurately simulating storm surge dynamics in regions with complex coastal topography. For operational forecasting in Hong Kong, China and similar environments, adopting a fully coupled wind-wave-current model offers clear advantages in reproducing peak water levels and reducing uncertainty in surge predictions.

5 Discussions

The wind-wave-current fully coupled model demonstrates superior skill in reproducing surged water levels, as it explicitly resolves the complex dynamic processes that

Table 3 RMSE and CC for Hato (2017) of water levels from Strats 1–3 at Tai Po Kau (TPK), Quarry Bay (QB), Tsim Bei Tsui (TBT), and the average

Hato (2017)		TPK	QB	TBT	Average
Strat. 1	RMSE (m)	0.26	0.25	0.33	0.28
	CC	0.94	0.94	0.93	0.94
Strat. 2	RMSE (m)	0.19	0.18	0.24	0.20
	CC	0.98	0.98	0.97	0.97
Strat. 3	RMSE (m)	0.11	0.14	0.14	0.13
	CC	0.98	0.99	0.99	0.99

Table 4 RMSE and CC for Mangkhut (2018) of water levels from Strats 1–3 at Tai Po Kau (TPK), Quarry Bay (QB), Shek Pik (SP), and the average

Mangkhut (2018)		TPK	QB	SP	Average
Strat. 1	RMSE (m)	0.27	0.19	0.19	0.22
	CC	0.95	0.98	0.96	0.96
Strat. 2	RMSE (m)	0.22	0.15	0.17	0.18
	CC	0.97	0.98	0.97	0.97
Strat. 3	RMSE (m)	0.18	0.13	0.14	0.15
	CC	0.98	0.99	0.98	0.98

govern coastal hydrodynamics. By contrast, storm surge models applied in previous studies have shown varying levels of accuracy depending on their coupling strategy, computational setup, and study region.

Compared with previously applied models, the wind-wave-circulation fully coupled system used in this study achieves RMSE on the order of ~10 cm, representing a substantial improvement in simulation accuracy. While simplified, uncoupled models such as SLOSH or ADCIRC have the advantage of reduced computational cost, advances in high-performance computing now make it feasible to run fully coupled models with significantly shorter CPU times than in the past. The ongoing development of GPU-based computation is expected to further consolidate this trend, offering the potential for real-time or near-real-time forecasting applications with higher physical fidelity. This shift highlights a broader trajectory in storm surge modeling: from computationally efficient but simplified approaches toward dynamically complete systems capable of resolving multi-scale interactions.

The effectiveness of coupled approaches has been confirmed in a number of recent studies. For example, Zhang et al. (2025) demonstrated that the FVCOM–SWAVE coupled model effectively captures the spatiotemporal evolution of typhoon waves and the joint distribution of wind speed and significant wave height in an offshore wind farm area, highlighting the advantages of coupled modeling for wave–current interaction studies. In the Pearl River Estuary, Luo et al. (2021) applied the SCHISM–WWM-III coupled system to simulate Super Typhoon Mangkhut in the Pearl River Estuary and showed that including wave effects improved the correlation with observations compared to uncoupled runs, highlighting the importance of surge-wave interactions for accurate modeling. Extending this perspective to climate change, Li et al. (2024) employed a high-resolution atmosphere–wave–ocean coupled model to examine tropical cyclone hazards in the Pearl River Delta under pseudo-global warming conditions, finding that future storms produce significantly higher surges and waves, underscoring the importance of coupled modeling frameworks in coastal risk assessment. In Hong Kong waters, Leung et al. (2024) reported surge simulation accuracies ranging from 0.23 to 0.58 m, which, while useful, remain less accurate than the ~0.10 m RMS errors achieved in this study.

Taken together, these investigations highlight that coupled models are indispensable for capturing the complex physics of storm surges, particularly in regions with intricate coastal topography such as estuaries, bays, and semi-enclosed harbors. Compared with these

Table 5 RMSE and CC for Higos (2020) of water levels from Strats 1–3 at Tai Miu Wan (TMW), Quarry Bay (QB), Tai Po Kau (TPK), Shek Pik (SP), Tai O (TO), Tsim Bei Tsui (TBT), and average

Higos (2020)		TMW	QB	TPK	SP	TO	TBT	Average
Strat. 1	RMSE (m)	0.15	0.15	0.15	0.15	0.13	0.16	0.15
	CC	0.98	0.98	0.97	0.98	0.99	0.98	0.98
Strat. 2	RMSE (m)	0.10	0.10	0.10	0.11	0.09	0.11	0.11
	CC	0.99	0.99	0.99	0.99	0.99	0.99	0.99
Strat. 3	RMSE (m)	0.08	0.08	0.08	0.09	0.08	0.09	0.08
	CC	0.99	0.99	0.99	0.99	1.00	0.99	0.99

Table 6 RMSE and CC for Kompasu (2021) of water levels from Strats 1−3 at Tai Miu Wan (TMW), Quarry Bay (QB), Tai Po Kau (TPK), Shek Pik (SP), Tai O (TO), Tsim Bei Tsui (TBT), and average

Kompasu (2021)		TMW	QB	TPK	SP	TO	TBT	Average
Strat. 1	RMSE (m)	0.21	0.20	0.23	0.18	0.16	0.18	0.19
	CC	0.94	0.95	0.95	0.97	0.98	0.98	0.96
Strat. 2	RMSE (m)	0.15	0.14	0.16	0.13	0.11	0.12	0.13
	CC	0.97	0.98	0.98	0.99	0.99	0.99	0.98
Strat. 3	RMSE (m)	0.12	0.11	0.13	0.10	0.09	0.10	0.11
	CC	0.98	0.99	0.99	0.99	0.99	0.99	0.99

Table 7 RMSE and CC for Saola (2023) of water levels from Strats 1−3 at Tai Po Kau (TPK), Quarry Bay (QB), Tai Po Kau (TPK), Shek Pik (SP), Tai O (TO), Tsim Bei Tsui (TBT), and average

Saola (2023)		QB	TPK	SP	TO	TBT	Average
Strat. 1	RMSE (m)	0.23	0.27	0.15	0.22	0.21	0.22
	CC	0.94	0.90	0.94	0.95	0.96	0.94
Strat. 2	RMSE (m)	0.15	0.18	0.13	0.14	0.15	0.15
	CC	0.95	0.92	0.95	0.96	0.96	0.95
Strat. 3	RMSE (m)	0.09	0.11	0.07	0.08	0.09	0.09
	CC	0.95	0.91	0.96	0.96	0.96	0.95

previous efforts, the present study demonstrates a higher level of accuracy in reproducing water levels across multiple typhoon cases in Hong Kong, China. Thus, with the supercomputer resources, the fully coupled model developed in this study can be used to implement real-time predictions of storm surge with high accuracy. The future work will focus on expanding the evaluation to a broader set of typhoon cases in order to further validate the robustness and accuracy of the system. In addition, efforts will be directed toward transforming the current framework into a fully operational platform, with the ultimate goal of integrating it into routine forecasting services for real-time storm surge prediction and coastal risk management.

Nevertheless, important challenges remain. Fully coupled models are highly sensitive to boundary conditions and the accuracy of atmospheric forcing, and their computational demands can still be prohibitive for simulations over very large domains or for ensemble-based probabilistic forecasting. With the rapid advances in machine learning and deep learning, however, new opportunities are emerging. Artificial intelligence (AI) techniques could be applied to storm surge modeling, either as stand-alone predictive tools or in hybrid approaches that integrate AI with traditional atmosphere-ocean-wave numerical models. In particular, deep learning offers promise for accelerating turbulent closure schemes, enhancing subgrid-scale parameterizations, and improving data assimilation, thereby complementing physically based models and reducing computational cost without sacrificing accuracy.

6 Conclusions

In this study, we developed a fully coupled wind-wave-circulation modeling system to simulate storm surge water levels in the coastal waters of Hong Kong, China within the Earth System Modeling Framework (ESMF). The system couples the Weather Research and Forecasting (WRF) model to provide atmospheric forcing, the Simulating Waves Nearshore (SWAN) model to resolve wave dynamics, and the Finite-Volume Community Ocean Model (FVCOM) to represent ocean circulation.

For comparison, both an uncoupled model, in which only wind forcing drives ocean currents and waves, and a partially coupled model, in which wind forcing is combined with wave-current interactions, were also evaluated. These three approaches were tested against observations for five major typhoon events that produced substantial storm surges in Hong Kong, China. Across these typhon events, the water level observations from the tidal gauges in Hong Kong coastal waters are used to

evaluate the model performance.

The timing and magnitude of peak water-level increases varied widely among stations, shaped by storm track, wind forcing, and coastal morphology. Tai Po Kau and Tai Miu Wan often showed the earliest peaks, while Tsim Bei Tsui consistently recorded the latest, reflecting north-westward surge advection. Event-specific maxima at Tai Po Kau, Shek Pik, and Tsim Bei Tsui highlight the role of local bay geometry in surge amplification. The irregular timing between stations further indicates that surge propagation in Hong Kong waters depends on complex hydrodynamic and storm-specific interactions rather than distance alone.

The comparisons show that the fully coupled model consistently provides the highest accuracy. Relative to the uncoupled system, root-mean-square errors (RMSEs) were reduced by 52.6% for Hato (2017), 31.3% for Mangkhut (2018), 43.0% for Higos (2020), 42.4% for Kompasu (2021), and 60.5% for Saola (2023). The degree of improvement varies across storms, reflecting differences in intensity, translation speed, track, and coastal morphology. The benefits of coupling are especially evident at Tai Po Kau in Tolo Harbour, a semi-enclosed site where wave reflection and current confinement amplify hydrodynamic interactions. At this location, RMSE reductions of 0.10−0.16 m are achieved, significantly larger than at open-coast stations, underscoring the importance of full coupling in narrow bays and estuaries.

From a process perspective, the findings confirm that uncoupled models cannot represent critical mechanisms such as wave-induced setup, current feedback on wave growth, and the modulation of wind stress by sea-state conditions, all of which strongly influence surge amplification. While the wave-current coupled system captures some of these interactions and improves performance, only the fully coupled framework reproduces peak surge levels with sufficient fidelity to match observations. Importantly, the RMSE of ~10 cm makes the fully coupled framework suitable for operational storm surge prediction in Hong Kong, China and other coastal regions with similarly complex dynamics.

Competing interests The authors declare that they have no competing interests.

Acknowledgments This study was supported by National Key R&D Program of China (No. 2021YFB3900400).

References

Booij N, Ris R C, Holthuijsen L H (1999). A third-generation wave model for coastal regions: 1. Model description and validation. J Geophys Res, 104(C4): 7649–7666

Bunya S, Dietrich J C, Westerink J J, Ebersole B A, Smith J M, Atkinson J H, Jensen R, Resio D T, Luettich R A, Dawson C, Cardone V J, Cox A T, Powell M D, Westerink H J, Roberts H J (2010). A high-resolution coupled riverine flow, tide, wind, wind wave, and storm surge model for southern Louisiana and Mississippi, Part I: Model development and validation. Mon Weather Rev, 138(2): 345–377

Cañizares R, Madsen H, Jensen H R, Vested H J (2001). Developments in operational shelf sea modelling in Danish waters. Estuar Coast Shelf Sci, 53(4): 595–605

Chen C, Beardsley R C, Cowles G (2006). An unstructured grid, finite-volume coastal ocean model (FVCOM) system. Oceanography (Wash DC), 19(1): 78–89

Chen C, Liu H, Beardsley R C (2003). An unstructured grid, finite-volume, three-dimensional, primitive equations ocean model: application to coastal ocean and estuaries. J Atmos Ocean Technol, 20(1): 159–186

Egbert G D, Erofeeva S Y (2002). Efficient inverse modeling of barotropic ocean tides. J Atmos Ocean Technol, 19(2): 183–204

Flowerdew J, Mylne K, Jones C, Titley H (2013). Extending the forecast range of the UK storm surge ensemble. Q J R Meteorol Soc, 139(670): 184–197

Forbes C, Rhome J, Mattocks C, Taylor A (2014). Predicting the storm surge threat of Hurricane Sandy with the National Weather Service SLOSH model. J Mar Sci Eng, 2(2): 437–476

Gerritsen H, de Vries J W, Philippart M (1995). The Dutch Continental Shelf Model. In: Lynch D, Davies A, eds. Quantitative Skill Assessment for Coastal Ocean Models. American Geophysical Union, Washington, DC

Glahn B, Taylor A, Kurkowski N, Shaffer W A (2009). The role of the SLOSH model in National Weather Service storm surge forecasting. National Weather Digest, 33(1): 3–14

Han X, Sheng J M, Pan X S, Liu S C, Li C H (2019). Study on the refined storm surge numerical model in the Southern Yellow Sea. Marine Forecasts, 36(1): 52–58 (in Chinese)

Hasegawa H, Kohno N, Hayashibara H (2012). JMA's storm surge prediction for the WMO Storm Surge Watch Scheme (SSWS). Technical Review No. 14, RSMC Tokyo – Typhoon Center, March 2012

Higaki M, Hayashibara H, Nozaki F (2009). Outline of the storm surge prediction model at the Japan Meteorological Agency. Technical Review No. 11, RSMC Tokyo – Typhoon Center, March 2009: 25–38

Hill C, DeLuca C, Balaji, Suarez M, Da Silva A (2004). The architecture of the Earth System Modeling Framework. Comput Sci Eng, 6(1): 18–28

Jelesnianski C P, Chen J, Shaffer W A (1992). SLOSH: Sea, Lake and Overland Surges from Hurricanes. NOAA Technical Report NWS 48, U.S. Department of Commerce

Kliem N, Nielsen J W, Huess V (2006). Evaluation of a shallow-water unstructured mesh model for the North Sea-Baltic Sea. Ocean Model (Oxf), 15(1−2): 124–136

Lau D S, Chan W S, Wong Y C, Lam C C, Chan P W (2024). Hindcast insights from storm surge forecasting of Super Typhoon Saola (2309) in Hong Kong with the sea, lake and overland surges

from hurricanes model. Atmosphere (Basel), 15(1): 17

Leung N C, Chow C K, Lau D S, Lam C C, Chan P W (2024). WRF-ROMS-SWAN coupled model simulation study: effect of atmosphere-ocean coupling on sea-level predictions under tropical cyclone and northeast monsoon conditions in Hong Kong. Atmosphere (Basel), 15(10): 1242

Li S, Chen C (2022). Air-sea interaction processes during Hurricane Sandy: coupled WRF-FVCOM model simulations. Prog Oceanogr, 206: 102855

Li Z, Fung J C H, Wong M F, Lin S, Cai F, Lai W, Lau A K H (2024). Future changes in intense tropical cyclone hazards in the Pearl River Delta region: an air-wave-ocean coupled model study. Nat Hazards, 120(8): 7139–7154

Liu Q, Dong J, Yu F, Fu C, Li M (2014). A high-resolution typhoon storm surge forecast model covering the whole China's coastal areas and its application. Acta Oceanolog Sin, 36(11): 30–37 (in Chinese)

Luettich R A, Westerink J J, Scheffner N W (1992). ADCIRC: an advanced three-dimensional circulation model for shelves, coasts and estuaries; Report 1: Theory and methodology of ADCIRC-2DDI and ADCIRC-3DL. Technical Report DRP-92–6, U.S. Army Engineer Waterways Experiment Station, Vicksburg, MS

Luo Z, Huang B, Chen X, Tan C, Qiu J, Huang G (2021). Effects of wave-current interaction on storm surge in the Pearl River Estuary: a case study of Super Typhoon Mangkhut. Front Mar Sci, 8: 692359

Masson S, Jullien S, Maisonnave E, Gill D, Samson G, Le Corre M, Renault L (2025). An updated non-intrusive, multi-scale, and flexible coupling interface in WRF 4.6. 0. Geosci Model Dev, 18(3): 1241–1263

McIvor A, Spencer T, Möller I, Spalding M (2012). Storm surge reduction by mangroves. The Nature Conservancy and Wetlands International. Available at: https://www.mangrovealliance.org/wp-content/uploads/2018/05/storm-surge-reduction-by-mangroves-1.pdf

Mellor G L, Yamada T (1982). Development of a turbulence closure model for geophysical fluid problems. Rev Geophys, 20(4): 851–875

Michalakes J G, Dudhia J, Gill D, Klemp J, Skamarock W (1998). Design of a next generation regional weather research and forecast model. In: Zwieflhofer W, Kreitz N, eds. Towards Teracomputing: Proceedings of the Eighth ECMWF Workshop on the Use of Parallel Processors in Meteorology. World Scientific, River Edge, NJ: 117–124

Muis S, Verlaan M, Winsemius H C, Aerts J C J H, Ward P J (2016). A global reanalysis of storm surges and extreme sea levels. Nat Commun, 7(1): 11969

Petersen C, Kmit M, Nielsen N W, Amstrup B, Huess V (2005). Performance of DMI-HIRLAM-T15 and DMI-HIRLAM-S05 and the storm surge model in winter storms. Technical Report 05–13, Danish Meteorological Institute, Ministry of Transport

Qi J, Chen C, Beardsley R C, Perrie W, Cowles G W, Lai Z (2009). An unstructured-grid finite-volume surface wave model (FVCOM-SWAVE): implementation, validations and applications. Ocean Model (Oxf), 28(1–3): 153–166

Skamarock W C, Klemp J B, Dudhia J, Gill D O, Barker D M, Duda M G, Huang X Y, Wang W, Powers J G (2019). A description of the Advanced Research WRF version 4 (ARW). NCAR Technical Note NCAR/TN-556+STR, National Center for Atmospheric Research, Boulder, CO

Sun K, Pan J (2023). Model of storm surge maximum water level increase in a coastal area using ensemble machine learning and explicable algorithm. Earth Space Sci, 10(12): e2023EA003243

Tasnim K, Koichiro O, Shibayama T, Esteban M, Nakamura R (2014). Numerical simulation of cyclonic storm surges over the Bay of Bengal using a meteorology-wave-surge-tide coupled model. In: Coastal Engineering Proceedings, 1(34): currents. 26

Verlaan M, Zijderveld A, de Vries H, Kroos J (2005). Operational storm surge forecasting in the Netherlands: developments in the last decade. Philosophical Transactions of the Royal Society A: Mathematical, Physical and Engineering Sciences, 363(1837): 1441–1453

Zhang B, Li X, Wang L, Gao Y (2025). Numerical simulation of typhoon waves in an offshore wind farm area of the South China Sea. J Mar Sci Eng, 13(3): 451